THE UNIVERSITY OF SYDNEY

SCHOOL OF CIVIL ENGINEERING

FRACTURE INVESTIGATION OF WELDED CRUCIFORM CONNECTIONS

RESEARCH REPORT R972

X LIU
S YAN
K J R RASMUSSEN
G G DEIERLEIN

February 2023

ISSN 1833-2781

Copyright Notice

School of Civil Engineering, Research Report R972
Fracture investigation of welded cruciform connections.
X Liu MScEng
S Yan PhD
K J R Rasmussen MScEng PhD Deng
G G Deierlein MScEng PhD
February 2023

ISSN 1833-2781

Published by:
School of Civil Engineering
The University of Sydney
Sydney NSW 2006
Australia

Abstract

As one of the main failure modes of steel structures, fracture in welded connections has widely been discussed based on experimental investigations and numerical simulations. However, the mechanical properties of the weld and Heat Affected Zone (HAZ), such as stress-strain relationships and fracture strains under various stress states, have rarely been considered in these analyses. Therefore, in this paper, the fracture process of welded connections is discussed to investigate the effects of the inhomogeneity of mechanical properties in the weld zone. Tensile tests are conducted on welded cruciform specimens fabricated using 8 mm or 12 mm fillet welds and finite element models are developed by considering or ignoring the material inhomogeneity in the weld zone. The simulation results are compared with the experimental and it is concluded that the assumption of homogenous properties within the weld zone using the properties of the base metal will underestimate the strength of the welded cruciform specimens and using the mechanical properties of the three material areas in the weld zone will increase the accuracy of the simulation results. Using the free parameters calibrated by the fracture strains of the three material areas, the fracture process of the welded cruciform specimens is simulated using the fracture model LMVGM, and the comparison shows that the mechanical properties of the weld and HAZ should be included in the investigation of fracture in welded connections to obtain reliable simulation results.

Keywords: Welded connections, fracture, mechanical properties, material inhomogeneity

Table of Content

1. Introduction

Welding is one of the most common methods in civil engineering for connecting steel components for its high manufacturing speed, flexibility and reliability with low costs [1]. In a welded connection, the steel components are connected by melting and fusing of the weld material and a portion of base metal. During this process, the high temperature and different cooling rates lead to locally different microstructures, inhomogeneous properties and residual stresses in the weld zone, which can then be divided into three material areas, base metal, weld and heat affected zone (HAZ) [2,3].

Fracture of welded connections is one of the primary failure modes in steel structures, and numerous experimental investigations have been carried out on simple specimens [4-7] or large-scale welded connections [8-13] to study their failure mode and fracture behaviour. The experimental results show that fracture always occurs in the weld or HAZ within the weld zone of the weld connection with large-scale plastic deformation [4-13]. However, in the analysis or finite-element (FE) simulations of welded connections, the mechanical properties of the weld and HAZ are normally assumed to be the same as those of the base metal [12,14-17] although the mechanical properties in the weld zone are inhomogeneous. This simplified assumption is due to the lack of experimental data related to mechanical properties of the weld and HAZ areas and may lead to inaccurate prediction of the performance of welded connections. Therefore, it is necessary to determine the mechanical properties of the three material areas in the weld zone for the investigation of the fracture performance of welded connections.

In some recent studies, the mechanical properties of the weld are measured and included in the numerical simulation of welded connections [5, 18]. Shi et al. [5] conducted coupon tests on rectangular specimens and smooth and notched round bars extracted from the weld and simulated the fracture process of a series of lap-welded joints using fracture models Void Growth Model (VGM) and Stress Modified Critical Strain Model (SMCS). Ran et al. [18] measured the fracture strains of the weld and base metal using smooth and notched round bars and rectangular notched specimens extracted from a butt-welded plate and it was found that weld has lower fracture ductility than the base metal. The fracture process of welded connections was simulated using the Bai-Wierzbicki model calibrated by the fracture strains of weld and base metal. In these studies, although the material inhomogeneity is considered in the numerical simulation, the mechanical properties of the HAZ area were still ignored.

In this paper, the fracture process of welded connections is discussed to investigate the effects of the inhomogeneity of mechanical properties in the weld zone. A series of welded cruciform specimens are fabricated using 8 mm or 12 mm fillet welds. Macroetching and hardness tests are then performed on the cross-sections of these specimens. After identifying the weld, HAZ and base metal areas in the weld zone, the width of HAZ and the values of the Vickers hardness for the three material areas are measured and the results are compared with those of butt-welded plates made using the same materials under the same welding process. Tensile tests are then conducted on the welded cruciform specimens. The experimental results, including load-deformation curves and fracture deformation, are discussed and compared between the two specimen types.

Finite element models are developed by considering or ignoring the mechanical properties of weld and HAZ in the weld zone, and the simulation results are compared with the experimental results to discuss the effect of material inhomogeneity in the weld zone.

2. Tests on fracture in welded cruciform specimens

2.1. Welded cruciform specimens

A series of cruciform specimens were designed and fabricated, as shown in Fig. 1. All plates forming the connections were extracted from a 20 mm thick AS350 grade steel plates [19]. In each welded connection, the supported plates were welded perpendicularly to the supporting plate through 12 mm fillet welds by three weld passes or 8 mm fillet welds by one weld pass, as shown in Fig. 1(a). The welded connections were made through gas metal-arc welding (GMAW). The welding wire was of grade B-G49 [20], and the shielding gas was 18% CO2 bal Ar. The welding voltage ranged from 23 to 26 V, the current ranged from 200 to 220 A, and the welding speed ranged from 200 to 250 mm/min, i.e. the heat input ranged from 1.10 to 1.71 kJ/mm. After removing the 40 mm long part from the edges to eliminate the run-on and run-out effects, four 10 mm thick slices were cut from the welded connections. These slices are named “cruciform specimens” in following sections, whose geometries are shown in Fig. 7-1(c). The letters “F8” and “F12” refer to the two specimen types cut from the long specimens with weld sizes of 8 mm or 12 mm, respectively.

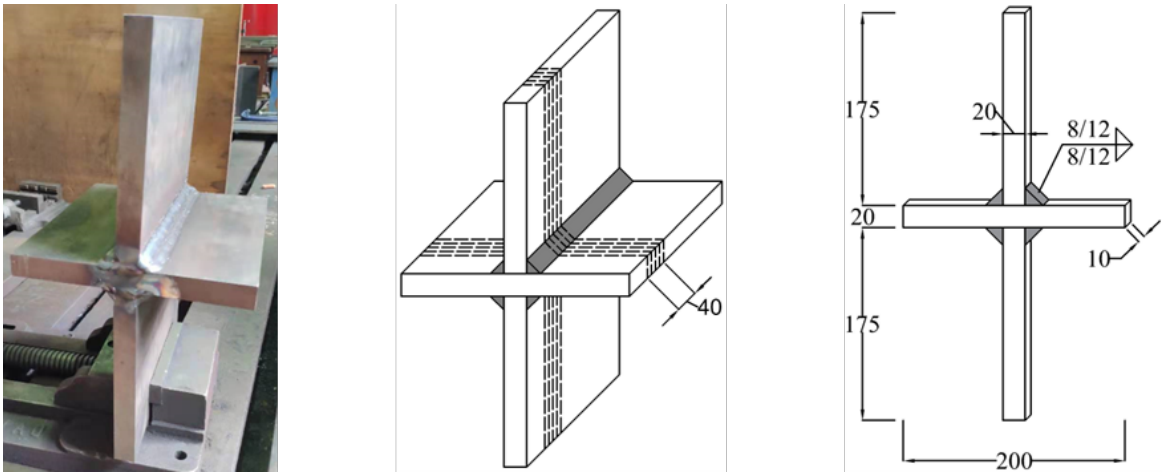

(a) Photo of a welded connection (b) Slices cut from a welded connection (c) Geometry of cruciform specimens

Fig. 1. Welded cruciform specimens (Dimensions in mm)

The surface of each cruciform specimen was macroetched, after which the dividing lines were determined, and the distribution of weld and HAZ could be distinguished. It is observed from the photo of the macroetched surface of an F12 specimen in Fig. 2 that the three weld passes in the 12 mm fillet welds formed curved dividing lines, and the width of HAZ was larger near the weld toe than the weld root. The weld area was always larger than the norminal size since the high temperature during the welding process melted the base metal near the edge allowing the weld area to blend into the supported and supporting plates.

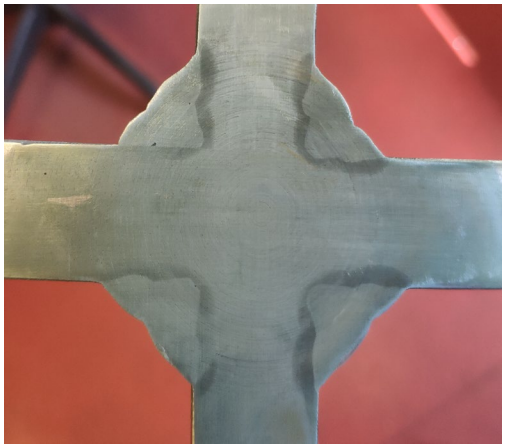

Fig. 2. Photo of the macroetched surface of a F12 specimen.

Two welds were chosen from each specimen type, and the width of HAZ and hardness of the three materials were then measured for these two welds. The widths of HAZ were measured as the horizontal distances between the two dividing lines on the supported plates and as the vertical distances on the supporting plates. For each weld, the HAZ widths were measured from four points at different distances from the weld root along the weld legs on the supported and supporting plates, resulting in a total of 32 measurements for both the F8 and F12 specimens, as shown in Fig. 3. The results of most measurement ranged from 1.5 mm to 3.0 mm, and the average width of the HAZ area was 2.28 mm.

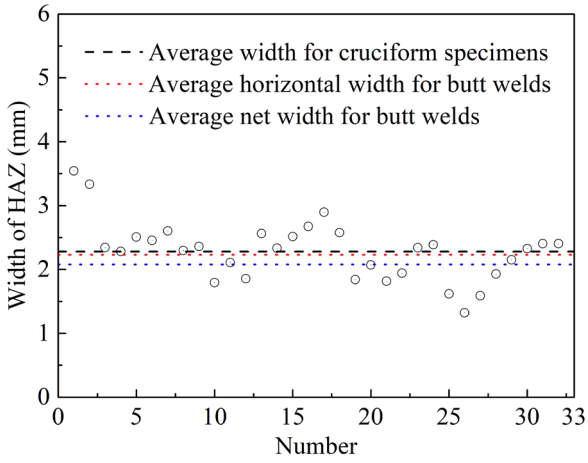

Fig. 3. Width of HAZ in the welded cruciform specimens.

The Vickers hardness was measured for these two welds for each specimen type using the Dura Scan machine at 15 locations, three in the weld area, six in the HAZ and six in the base metal area. The three locations in each material area from each piece were randomly selected, and the distance between each location was large enough that they did not interact with each other. Under the load of 4.9 N (0.5 kg), the average indentation sizes were 78.07 μm, 70.78 μm and 65.25 μm, and the average HV0.5 values were computed as 152.16, 185.41 and 217.83, for the base metal, HAZ and weld, respectively. The hardness of the three material areas was plotted in Fig. 4, where letters “FW-8” and “FW-12” refer to 8 mm fillet welds, and 12 mm fillet welds, respectively. The test results show that the weld had the highest hardness while the base metal was the softest.

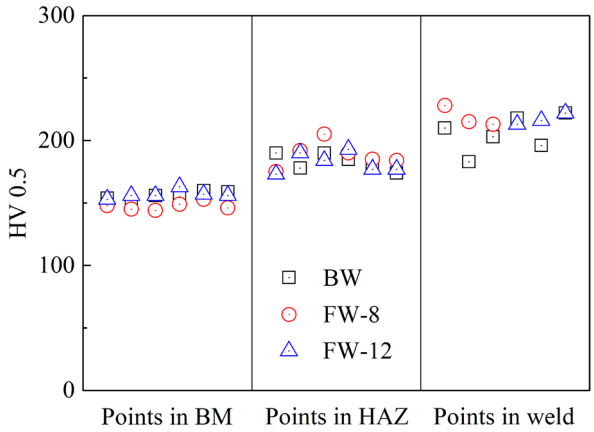

Fig. 4. Hardness results of cruciform specimens.

2.2. Mechanical properties of base metal, weld and HAZ in the weld zone

In [21], the stress-strain relationships and fracture strains of base metal, weld and HAZ were measured by conducting tensile tests on miniature flat plates, notched round bars and grooved plates extracted from the three material areas of butt-welded plates. The components of the butt-welded plates were cut from the same steel plate and were made under the same welding process as those of the cruciform specimens. The width of HAZ and the hardness of the three material areas measured from the cruciform specimens were compared with those measured from the butt-welded plates in Figs. 3 and 4, where letter "BW" refers to butt welds. The comparison shows that the width of HAZ measured from the cruciform specimen was close to the average horizontal HAZ width measured from the butt-welded plates and the values of hardness of the three material areas in the weld zone measured from the cruciform specimens are consistent with those of the butt-welded plates. Therefore, it is concluded that under the same welding process, the widths of HAZ measured from different specimen types made using the same materials will be similar. Considering the hardness of steel is related to its mechanical properties, it is indicated that the mechanical properties of the three material areas in the cruciform specimens were similar to those in the butt-welded plates. Therefore, the results of the stress-strain relationships (Fig. 5) and fracture strains of the weld, HAZ and base metal (Table 1) measured in [21] were then used in the simulation of welded cruciform specimens in the following sections. The stress states of the miniature coupons were characterised by the stress triaxiality, T, and Lode angle parameter, ξ. The two parameters are the normalised first invariant of the stress tensor, I_1, and the normalised third invariant of the stress deviator tensor, J_3, respectively:

$$T = \frac{I_1}{3\bar{\sigma}} \tag{1}$$

$$\xi = \frac{27 J_3}{2\bar{\sigma}^3}, \tag{2}$$

where $\bar{\sigma}$ is the von Mises stress. ξ relates to the Lode angle, θ, through:

$$\xi = \cos(3\theta). \tag{3}$$

Since the range of θ is between 0 and $\pi/3$, ξ ranges between -1 and 1. Considering the values of T and ξ normally did not stay constant during plastic loading, their average values over the loading history should be used as the representative values, which are calculated as:

$$T_{\text{avg}} = \frac{1}{\varepsilon_{\text{f}}}\int_0^{\varepsilon_{\text{f}}} T d\varepsilon_{\text{p}} \tag{4}$$

$$\xi_{\text{avg}} = \frac{1}{\varepsilon_{\text{f}}}\int_0^{\varepsilon_{\text{f}}} \xi d\varepsilon_{\text{p}}\,, \tag{5}$$

where ε_{f} and ε_{p} are the fracture strain and equivalent plastic strain, respectively.

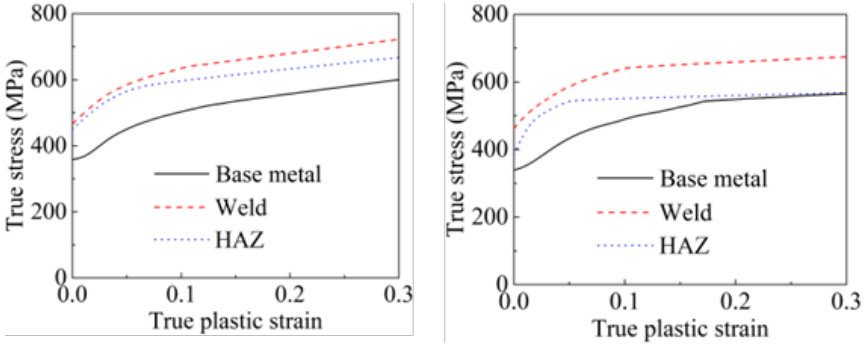

(a) Longitudinal (b) Transverse

Fig. 5. Stress-strain curves.

Table 1. Stress states and fracture strains of miniature coupons.

		FP			NRB			GP		
		T_{avg}	ξ_{avg}	ε_{f}	T_{avg}	ξ_{avg}	ε_{f}	T_{avg}	ξ_{avg}	ε_{f}
Longitudinal	Base metal	0.40	0.97	0.82	1.04	1.00	0.18	1.08	0.47	0.10
	Weld	0.44	0.93	0.94	1.13	1.00	0.42	1.18	0.16	0.18
	HAZ	0.44	0.94	0.80	1.14	1.00	0.18	1.16	0.27	0.11
Transverse	Base metal	0.49	0.89	0.90	1.08	1.00	0.61	1.10	0.18	0.32
	Weld	0.49	0.91	0.69	1.20	1.00	0.50	1.18	0.18	0.19
	HAZ	0.59	0.77	0.78	1.25	1.00	0.62	1.20	0.04	0.41

2.2. Test setup and experimental results

Tensile tests were conducted on the welded cruciform specimens to investigate their fracture process. The tests were performed in a 300 kN MTS Sintech testing machine, and four replicated tests were carried out for each specimen type. The photos of the test setup of the F8 and F12 specimens are shown in Fig. 6. To measure the deformation during the loading process, a pair of special clamps were fixed on the supported branches, and two displacement meters were fixed on the clamps. The deformation of the specimen was then obtained by averaging the measured results of the two displacement meters. The distance between the two clamps was 90 mm, which was termed the gauge length for the cruciform specimens. To obtain the static load-deformation curves, the loading was controlled at a low speed of 2 mm/min and paused three times for 100s to allow stress

relaxation. The static load-deformation curves were then converted from the original quasi-static curves following the same method adopted in [22].

(a) Unloaded F8 specimen

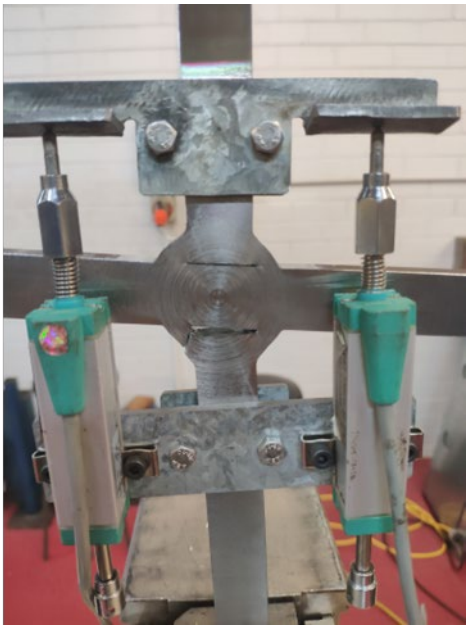

(b) Fractured F8 specimen

(c) Unloaded F12 specimen

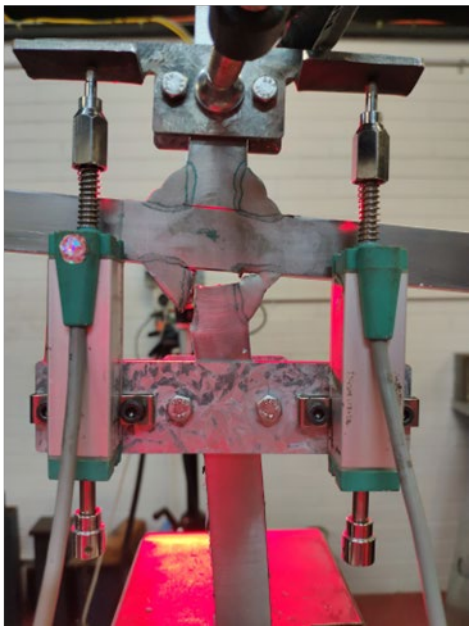

(d) Fractured F12 specimen

Fig. 6. Stress-strain curves.

The photos of the fractured F8 and F12 specimens are shown in Figs. 7 and 8, where the first crack was noted in the black circle. It is observed that a plastic deformation developed and localized in the weld zone during the loading process, and the first crack initiated from one weld root before a decrease in the loading capacity occurred. The crack propagated horizontally for a small distance, and a vertical crack was then formed, leading to the final fracture of the weld. The exceptions are the F8-1 specimen, whose first crack propagated horizontally along the fusion line, and the F12-2 specimen, whose first crack propagated to the

middle of the weld leg and then propagated vertically in the weld area. After the weld totally fractured due to the first crack, another crack occurred in the other weld on the same supported branch leading to the final failure of the cruciform specimen. It is shown that generally, the first crack of the cruciform specimens formed vertically in the weld zone, while the second crack formed in the weld zone horizontally or at an angle of about 45°.

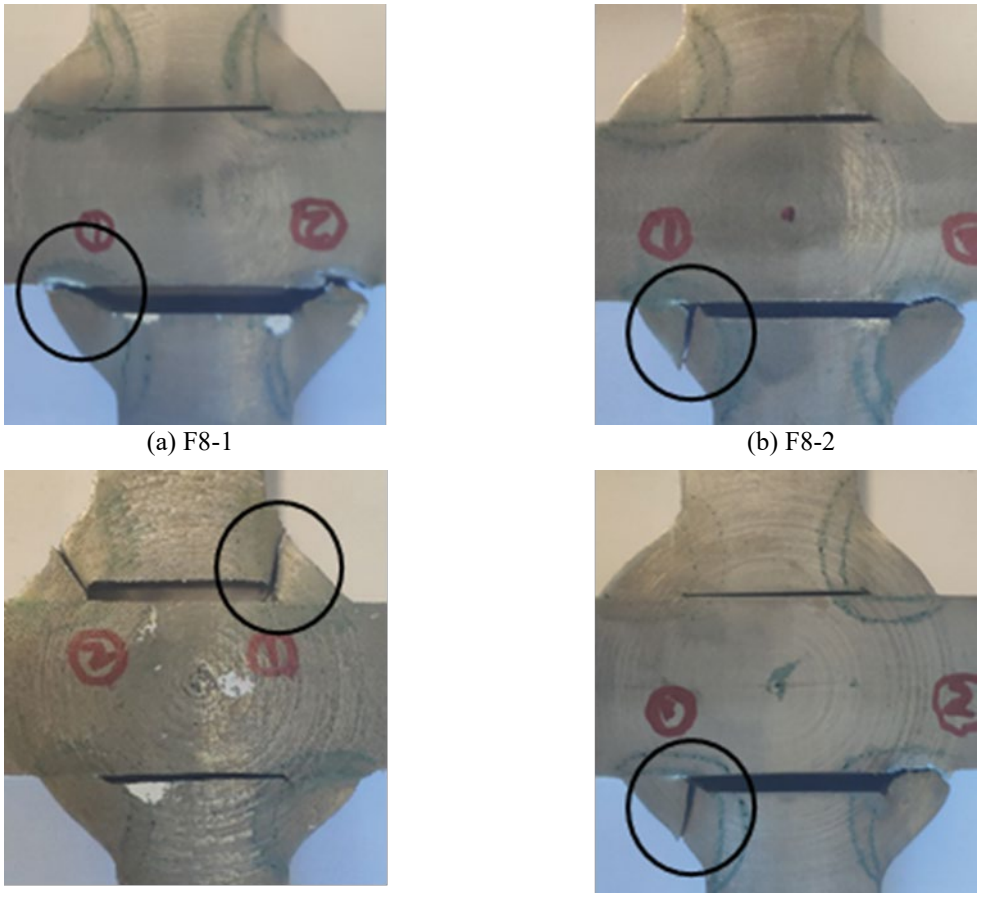

(a) F8-1 (b) F8-2

(c) F8-3 (d) F8-4

Fig. 7. Photos of fractured F8 specimens.

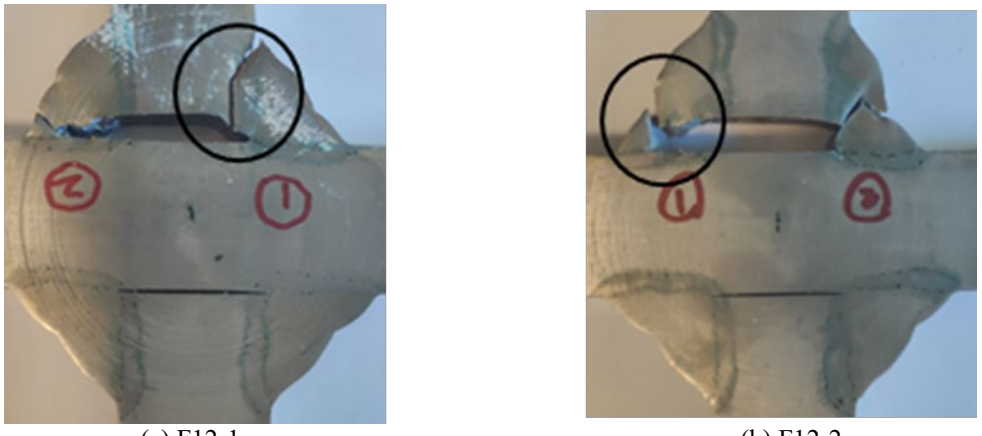

(a) F12-1 (b) F12-2

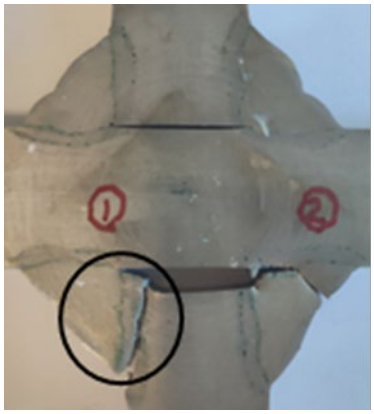

(c) F12-3

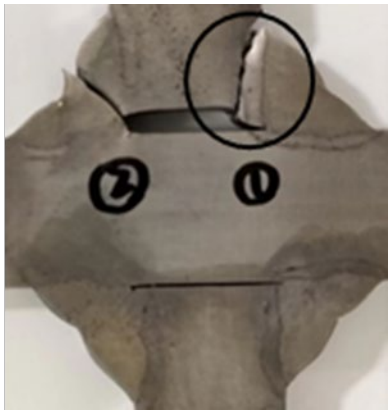

(d) F12-4

Fig. 8. Photos of fractured F12 specimens.

The load-deformation curves of the specimens are plotted in Fig. 9. It is observed that the results of the replicated tests for the F8 and F12 specimens were consistent with each other. The curves of the F8 specimens consistently increased to the maximum load after the elastic range and then decreased gradually to final failure, while the F12 specimens experienced a yield plateau stage before the increase, and the post-ultimate curves dropped more sharply. The maximum load, P_{max}, and the fracture deformation (the deformation under which first crack formed), D_f, are summarized in Table 2. The average maximum load and average fracture deformation of the F12 specimens were 84.44 kN and 5.54 mm, and were much larger than those of the F8 specimens, which were 51.39 kN and 2.17 mm. Considering that the thickness of the supporting and supported plates was the same in the two specimen types, the difference in their strength and ductility was caused by the different weld sizes.

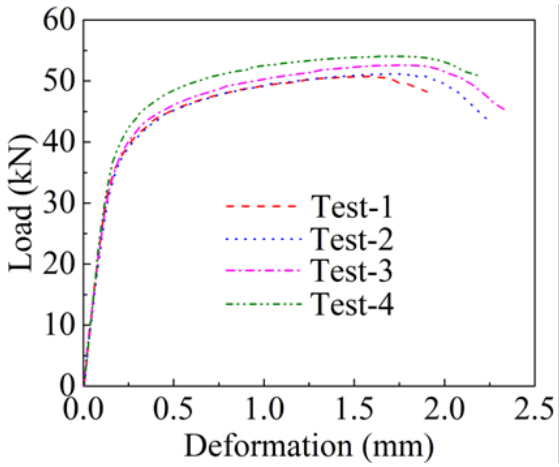

(a) F8

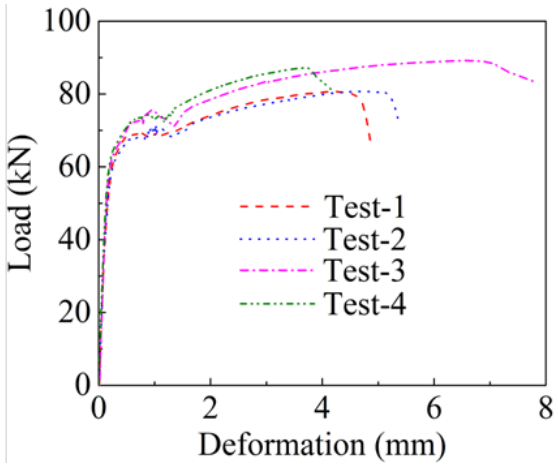

(b) F12

Fig. 9. Load-deformation curves of cruciform specimens.

Table 2. Maximum loads and fracture deformations of cruciform specimens.

	P_{max} (kN)	D_f (mm)		P_{max} (kN)	D_f (mm)
F8-1	47.75	1.92	F12-1	80.68	4.88
F8-2	51.16	2.24	F12-2	80.71	5.36
F8-3	52.59	2.35	F12-3	89.16	7.77
F8-4	54.06	2.18	F12-4	87.19	4.16
F8-avg	51.39	2.17	F12-avg	84.44	5.54

3. Numerical simulation of fracture in welded cruciform specimens

3.1. Simulation considering the mechanical properties of weld and HAZ

In order to simulate the test process, three-dimensional FE models were developed for the F8 and F12 specimens using ABAQUS, as shown in Fig. 10. Since the geometry of the specimen was symmetric, one-eighth of the specimen was modelled using eight-node linear solid elements with reduced integration (C3D8R). Considering the fracture occurred within the weld zone, the mesh size in the critical area was set to be 0.2 mm, while the element size of other parts of the specimen was 2 mm. The stress-strain relationships of the three material areas (Fig. 5) measured from the butt-welded plates in [21] were used in the simulation of the welded cruciform specimens.

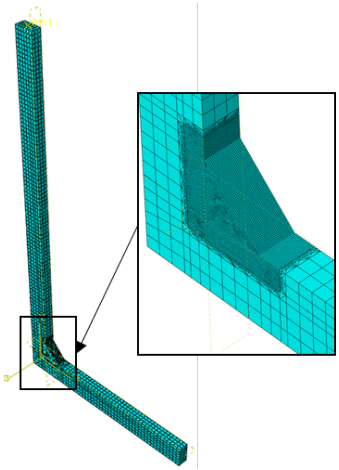

Fig. 10. Numerical model for cruciform specimens.

Three FE models were established for each specimen type to investigate the effect of the material heterogeneity within the weld zone, as shown in Fig. 11. In the first model, FEM-B, the mechanical properties within the weld zone were assumed to be homogenous, and the stress-strain relationship of the base metal was used for the whole FE model, as shown in Fig. 11(a). In the second model, FEM-BW, the mechanical properties of the weld were used in the weld area, while other parts adopted the properties of the base metal, as shown in Fig. 11(b). In the third model, FEM-BWH, in addition to adopting the properties of the weld, the mechanical properties of the HAZ were used for the HAZ area near the weld, and the width of the HAZ was

assumed to be the same as the horizontal width measured from the butt-welded plates, which was 2.23 mm, as shown in Fig. 11(c).

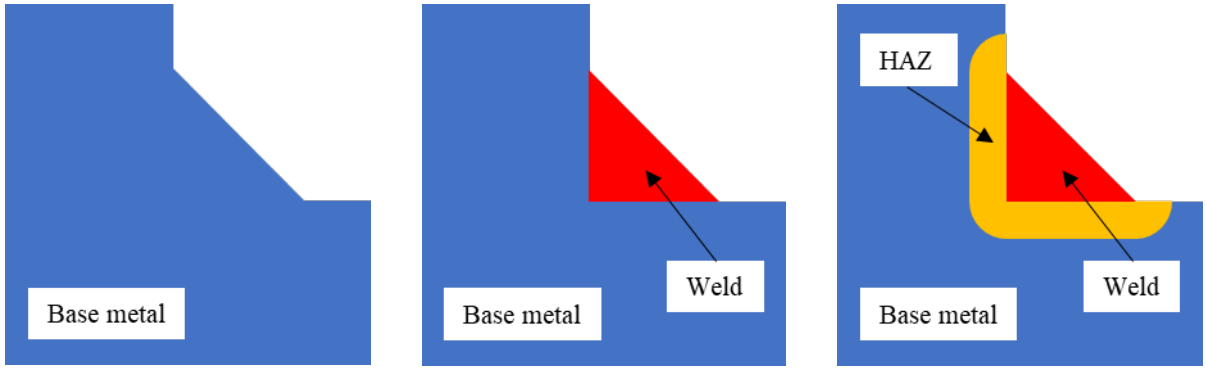

(a) FEM-B (b) FEM-BW (c) FEM-BWH

Fig. 11. Material areas in the weld zone.

The load-deformation curves simulated using the three FE models for the F8 and F12 specimens are plotted in Fig. 12. It is observed that without defining fracture models in the FE models, the FE curves do not drop due to the onset of fracture and continue to develop into a very large deformation. The simulated curves of the FEM-B models were always lower than the test results, showing that assuming the stress-strain relationships of the weld and HAZ were the same as those of the base metal would underestimate the strength of the welded cruciform specimens. The simulated curves of the FEM-BW models were higher than the results of the FEM-B models but were still slightly lower than the test curves, showing that considering the mechanical properties of the weld area would increase the accuracy of the simulation results. The simulated curves of the FEM-BWH models were higher than the results of both the FEM-B and FEM-BW models, and it is observed that the difference between the results of the FEM-BWH models and the FEM-BW models decreased with increasing deformation. The FEM-BWH models provided the simulation results with the best agreement with the test results. Therefore, it is concluded that the material heterogeneity within the weld zone has a significant effect on the simulation results of the welded cruciform specimens and using the different stress-strain relationships of the three material areas in the FE models will increase the accuracy of the simulation results.

The von Mises stress contours of the FEM-BWH models corresponding to the deformation of the gauge length equal to the fracture deformation are plotted for the two specimen types in Figs. 13. A non-uniform distribution of the von Mises stresses with large plastic deformation in the weld zone is observed with the stresses concentrating near the weld root and weld toe of the vertical fusion line.

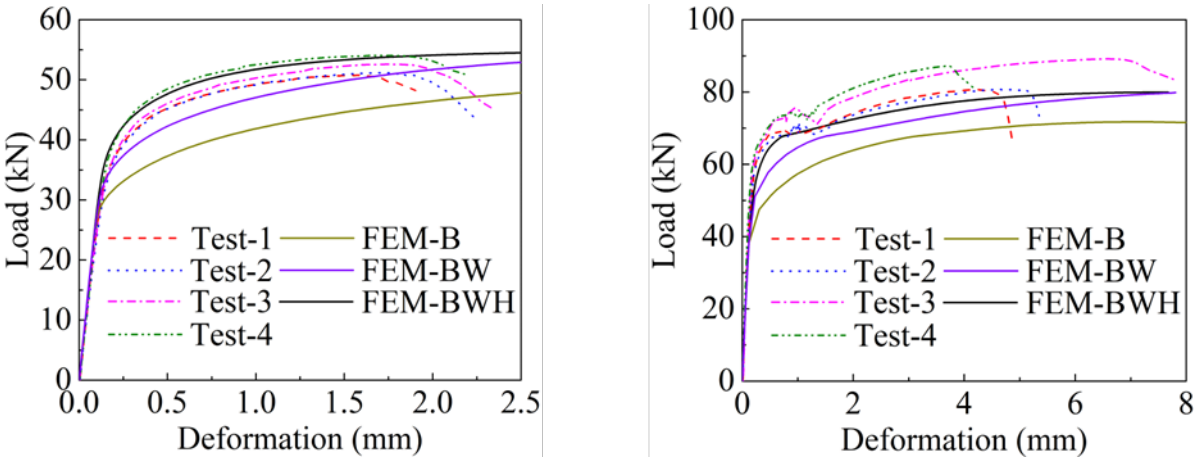

(a) F8 (b) F12

Fig. 12. Load-deformation curves considering material properties of three material areas.

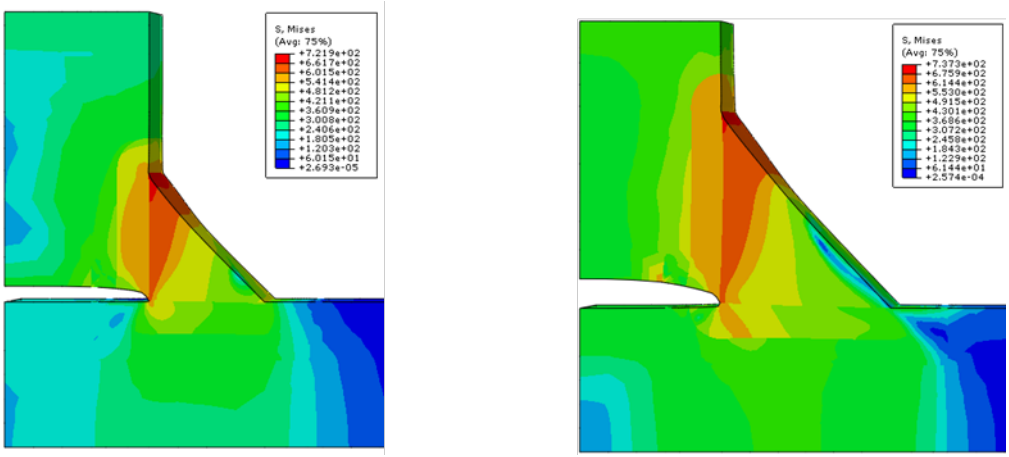

(a) F8 (b) F12

Fig. 13. Von Mises stress distribution of FEM-BWH models.

3.2. Simulation considering the fracture strains of weld and HAZ

After discussing the effect of the material heterogeneity in the simulation of the welded cruciform specimens, the fracture model LMVGM [23] was used to simulate the fracture process of the F8 and F12 specimens in the FE models by employing the user subroutine VUSDFLD in ABAQUS. The fracture strains of the three material areas in the weld zone under various stress states, including the axisymmetric tension states with high or medium stress triaxiality and the plane strain tension states, were obtained from the tensile tests on the miniature FPs, NRBs and GPs extracted from the butt-welded plates in [21]. As discussed in Section 2.1, the fracture strains measured from the butt-welded plates were used in the simulation of the welded cruciform specimens.

The stress triaxiality T, the Lode angle parameter ξ, and the fracture strain ε_f summarized in Table 1 were used to calibrate the free parameters of the fracture model LMVGM, as shown in Table 3. Based on the different fracture strains of the three material areas in the weld zone, the FEM-BWH models shown in Fig. 10(c) were developed for the F8 and F12 specimens using the calibrated LMVGM to predict the fracture

initiation and propagation. During the simulated loading process, the LMVGM was implemented in the VUSDFLD subroutine. In each step increment, the stress and strain tensors were first obtained and used to calculate the stress triaxiality and the Lode angle parameter. The value of the damage index D was then calculated using

$$D = \int_{\varepsilon_p} \frac{1}{\alpha} \cdot e^{\beta \cdot T - \gamma \cdot \xi} d\varepsilon_p \tag{6}$$

where α, β and γ are free parameters. When D reached unity, the fracture was predicted to initiate. Finally, the elements that reached the fracture criterion were deleted to simulate the propagation of the fracture.

Table 3. Fracture parameters of LMVGM.

		α	β	γ
Longitudinal	BM	0.97	2.44	0.84
	Weld	0.72	1.27	0.89
	HAZ	1.21	2.23	0.62
Transverse	BM	0.67	0.79	0.75
	Weld	0.32	0.62	1.17
	HAZ	0.73	0.51	0.47

The von Mises stress contours of the F8 and F12 specimens were plotted at various stages during the simulated loading process in Figs. 14 and 15. It is shown that the fracture initiation, propagation, and final failure of the weld zone were captured by the FEM-BWH models. Before the fracture initiation, the stress concentrated in the weld zone near the vertical fusion line, as shown in Figs. 14(a) and 15(a). The fracture then initiated from the weld root, which was consistent with the experimental observation, as shown in Figs. 14(b) and 15(b). After that, the fracture propagated in the weld zone, as shown in Figs. 14(c) and 15(c), which led to the final failure of the specimen, as shown in Figs. 14(d) and 15(d). The simulated fracture initiation and propagation process of the F8 and F12 specimens agreed well with the photos of the fractured specimens in Figs. 7(c) and 8(b). The simulated load-deformation curves were compared with the test curves in Fig. 16, and it is shown that the simulated curves for both the F8 and F12 specimens agreed well with the test results. Therefore, it is concluded that the fracture process can be captured by adopting the mechanical properties of the base metal, weld and HAZ in the weld zone using the fracture model LMVGM.

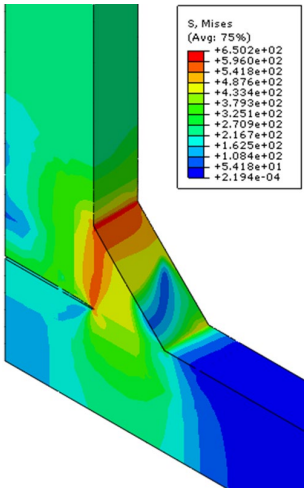

(a) Unfractured specimen

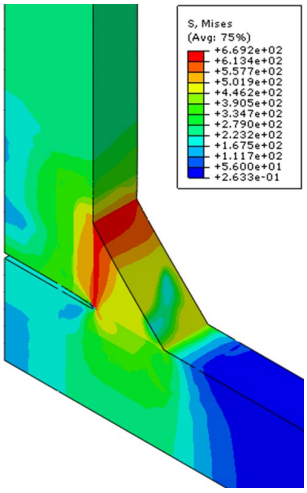

(b) Fracture initiation

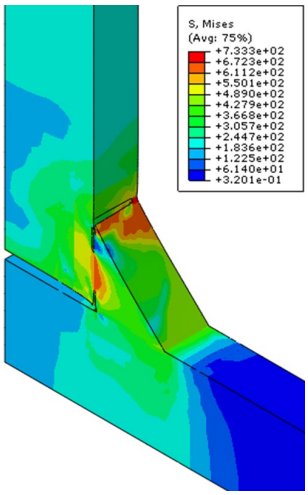

(c) Fracture propagation

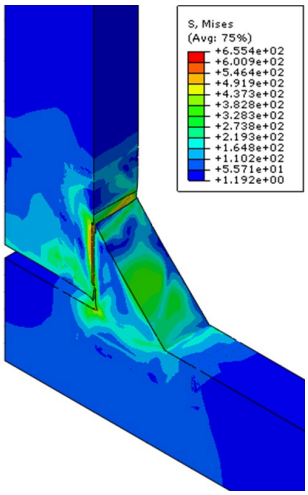

(d) Complete fracture

Fig. 14. Simulated fracture process of the F8 specimen (Von Mises stresses).

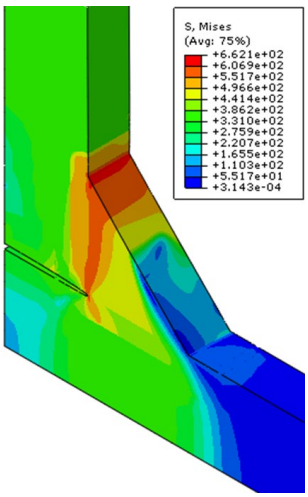

(a) Unfractured specimen

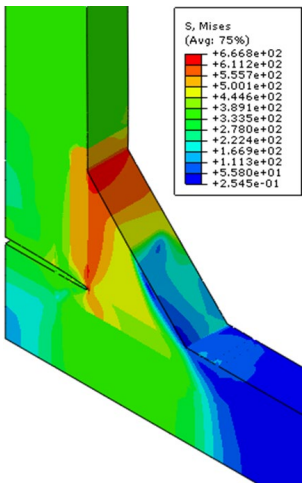

(b) Fracture initiation

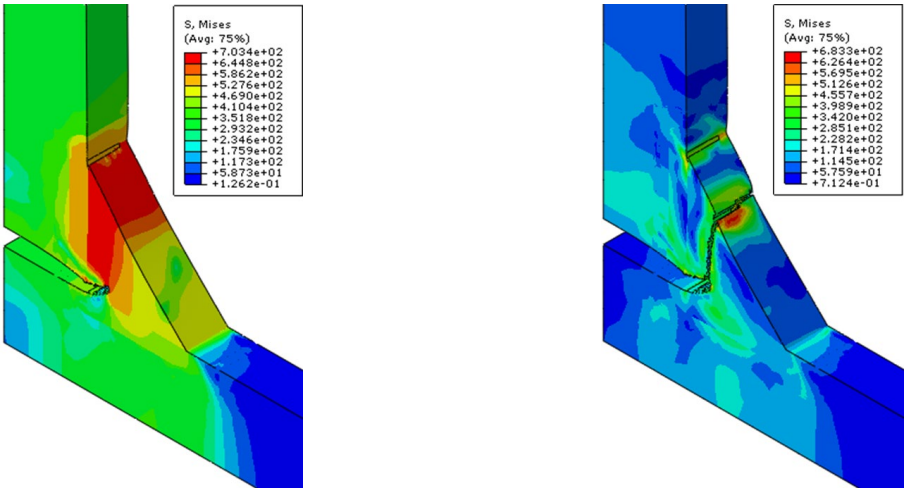

(c) Fracture propagation (d) Complete fracture

Fig. 15. Simulated fracture process of the F12 specimen (Von Mises stresses).

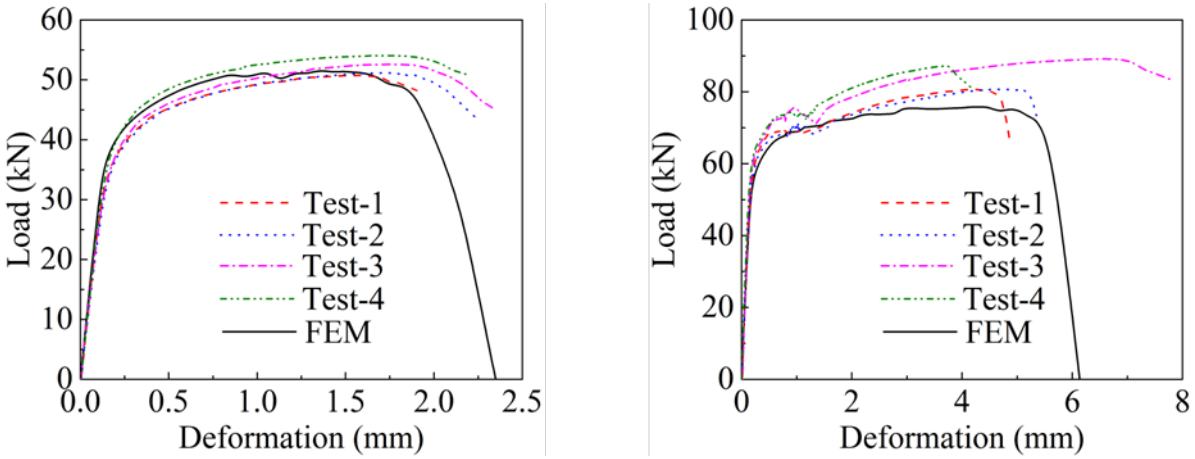

(a) F8 (b) F12

Fig. 16. Load-deformation curves considering fracture process.

4. Conclusions

In this paper, the fracture process of the cruciform specimens with 8 mm fillet welds (F8) or 12 mm fillet welds (F12) was experimentally investigated, and the fracture process was simulated using the fracture model LMVGM through the user subroutine VUSDFLD in ABAQUS.

The width of the HAZ was measured from the macroetched cruciform specimens, the average value of which was similar to the average value of the HAZ horizontal width measured from the butt-welded plates made of the same materials under the same welding process. The Vickers hardness of the base metal, weld and HAZ measured from the welded cruciform specimens was also consistent with those measured from the butt-welded plates. Therefore, it is concluded that the properties within the weld zone were similar among different specimen types made using the same materials under the same welding process. Tensile tests were conducted on the F8 and F12 specimens, and the test results showed that the plastic deformation developed and localized in the weld zone, and the fracture initiated from one weld root and generally propagated near the

vertical fusion line. The average maximum load and fracture deformation of the F12 specimens were higher than those of the F8 specimens.

The loading process of the cruciform specimens was simulated to investigate the effect of material heterogeneity within the weld zone. The mechanical properties of the base metal, weld and HAZ measured from the butt-welded plates were used in the simulation of welded cruciform specimens considering the values of their hardness were consistent with each other. Three FE models were developed by assuming the stress-strain relationships of the weld and HAZ were the same as the base metal (FEM-B), adopting the properties of the weld (FEM-BW) or the properties of both the weld and HAZ (FEM-BWH).

The FEM-BWH models provided results that agreed well with the test results, while the simulated curves of the FEM-B and FEM-BW models were lower than the test curves. It is shown that using the mechanical properties of the three material areas in the weld zone will increase the accuracy of the simulation results. Therefore, the material heterogeneity within the weld zone has a significant effect on the simulation results of the welded cruciform specimens, and the assumption of homogenous properties within the weld zone using the properties of the base metal will underestimate the strength of the welded cruciform specimens. The fracture process of the F8 and F12 specimens was simulated using the fracture model LMVGM with the free parameters calibrated using the fracture strains under various stress states measured for the weld, HAZ and base metal. The fracture initiation and propagation were simulated by deleting the elements that reached the fracture criterion using the user subroutine VUSDFLD in ABAQUS. The simulated load-deformation curves agreed well with the test results, and it is concluded that the fracture process of the welded connections can be simulated by considering the mechanical properties of the base metal, weld and HAZ in the weld zone using the fracture model LMVGM.

References

[1] Zerbst, U., Ainsworth, R.A., Beier, H.T., Pisarski, H., Zhang, Z.L., Nikbin, K., Nitschke-Pagel, T., Münstermann, S., Kucharczyk, P. and Klingbeil, D., 2014. Review on fracture and crack propagation in weldments–A fracture mechanics perspective. *Engineering fracture mechanics*, *132*, pp.200-276.

[2] Pham, T.H. and Kim, S.E., 2015. Determination of mechanical properties in SM490 steel weld zone using nanoindentation and FE analysis. *Journal of Constructional Steel Research*, *114*, pp.314-324.

[3] Ma, Y., Takikawa, A., Nakanishi, J., Doira, K., Shimizu, T., Lu, Y. and Ma, N., 2021. Measurement of local material properties and failure analysis of resistance spot welds of advanced high-strength steel sheets. *Materials & Design*, *201*, p.109505.

[4] Coelho, A.M.G., Bijlaard, F.S., Gresnigt, N. and da Silva, L.S., 2004. Experimental assessment of the behaviour of bolted T-stub connections made up of welded plates. *Journal of constructional Steel research*, *60*(2), pp.269-311.

[5] Shi, G. and Chen, Y., 2018. Investigation of ductile fracture behavior of lap-welded joints with 460 MPa steel. *Advances in Structural Engineering*, *21*(9), pp.1376-1387.

[6] Kanvinde, A.M., Gomez, I.R., Roberts, M., Fell, B.V. and Grondin, G.Y., 2009. Strength and ductility of fillet welds with transverse root notch. *Journal of Constructional Steel Research*, *65*(4), pp.948-958.

[7] Ran, M.M., Sun, F.F., Li, G.Q. and Wang, Y.B., 2021. Mechanical behaviour of longitudinal lap-welded joints of high strength steel: Experimental and numerical analysis. *Thin-Walled Structures*, *159*, p.107286.

[8] Ma, X., Wang, W., Chen, Y. and Qian, X., 2015. Simulation of ductile fracture in welded tubular connections using a simplified damage plasticity model considering the effect of stress triaxiality and Lode angle. *Journal of Constructional Steel Research*, *114*, pp.217-236.

[9] Liao, F., Wang, W. and Chen, Y., 2015. Ductile fracture prediction for welded steel connections under monotonic loading based on micromechanical fracture criteria. *Engineering Structures*, *94*, pp.16-28.

[10] Yaghoubshahi, M., Sun, M. and Tousignant, K., 2019. Design of fillet welds in RHS-to-RHS moment T-connections under branch in-plane bending. *Journal of Constructional Steel Research*, *159*, pp.122-133.

[11] Zhu, C., Rasmussen, K.J.R., Yan, S. and Zhang, H., 2019. Experimental full-range behavior assessment of bolted moment end-plate connections. American Society of Civil Engineers.

[12] Yelek, İ., Ardalı, R. and Yılmaz, İ., 2021. Fracture investigation of different welded steel beam-column connections under three-point bending test. *Journal of Constructional Steel Research*, *187*, p.106945.

[13] Qu, X., Qin, C., Sun, G. and Xie, Y., 2022, September. Research on fracture of steel structure welded joint based on micro-mechanism. In *Structures* (Vol. 43, pp. 434-448). Elsevier.

[14] Wang, Y., Zhou, H., Shi, Y. and Xiong, J., 2011. Fracture prediction of welded steel connections using traditional fracture mechanics and calibrated micromechanics based models. *International Journal of Steel Structures*, *11*, pp.351-366.

[15] Ghaderi-Garekani, M. and Maleki, S., 2022, November. An investigation of shear failure in welded channel and angle brace members. In *Structures* (Vol. 45, pp. 1287-1306). Elsevier.

[16] Chen, H., Shi, Y.J. and Wang, Y.Q., 2004. Fracture toughness properties of moment resistant column-beam connections Part II: inelastic analysis. *International Journal of Steel Structures*, *4*(1), pp.9-14.

[17] Song, Q.Y., Heidarpour, A., Zhao, X.L. and Han, L.H., 2018. Experimental and numerical investigation of ductile fracture of carbon steel structural components. *Journal of Constructional Steel Research*, *145*, pp.425-437.

[18] Ran, M.M., Zhong, Y.C., Wang, Y.Z., Li, G.Q., Xiong, F. and Ge, Q., 2022. Fracture prediction in transverse fillet welded joints of high strength structural steel. *Journal of Constructional Steel Research*, *189*, p.107101.

[19] AS/NZS 3678. Structural Steel–Hot-rolled plates, floor plates and slabs. Standards Australia, Sydney; 2011.

[20] AS/NZS 1554. Structural steel welding. Standards Australia, Sydney, 2014.

[21] Liu, X., S. Yan, K.J.R. Rasmussen, and G.G. Deierlein, Strengths and fracture strains of weld and HAZ in welded connections. February 2023, Research Report No. 973, School of Civil Engineering, University of Sydney: Sydney

[22] Huang, Y. and Young, B., 2014. The art of coupon tests. *Journal of Constructional Steel Research*, *96*, pp.159-175.

[23] Liu, X., Yan, S., Rasmussen, K.J.R. and Deierlein, G.G., 2022. Experimental investigation of the effect of Lode angle on fracture initiation of steels. *Engineering Fracture Mechanics*, *271*, p.108637.